


Inducing high- T_c ferromagnetism in the van der Waals crystal $\text{Mn}(\text{ReO}_4)_2$ via charge doping: A first-principles study

Ben-Chao Gong^{1,2,*}, Huan-Cheng Yang^{1,2,*}, Jian-Feng Zhang^{1,2}, Kai Liu^{1,2,†} and Zhong-Yi Lu^{1,2,‡}
Department of Physics and Beijing Key Laboratory of Opto-electronic Functional Materials & Micro-nano Devices, Renmin University of China, Beijing 100872, China

 (Received 2 May 2021; revised 21 June 2021; accepted 3 August 2021; published 18 August 2021)

Magnetic van der Waals (vdW) materials, which can serve as ideal platforms to study low-dimensional magnetism and possess potential applications in next-generation spintronic devices, have attracted intensive attention recently. Here, based on density functional theory calculations we predict that the electron-doped $\text{Mn}(\text{ReO}_4)_2$ (MRO) with an undulating layered structure is a ferromagnetic (FM) vdW material. Our calculations show that the magnetic interaction between two nearest-neighbor Mn atoms in the undoped MRO is very weak due to the long distance between the Mn atoms separated by the nonmagnetic ReO_4 tetrahedra. With moderate electron doping from charge injection or K intercalation, the Re atoms become spin polarized. Thus, an effective FM coupling between the Mn atoms can be induced via the Mn-O-Re antiferromagnetic superexchange, while the calculated T_c can exceed room temperature. The electron-doped MRO not only takes the advantage of strong FM interaction as double perovskites, but also avoids the shortage of the antisite disorder. The calculated small cleavage energy and stable phonon spectra indicate that MRO can be exfoliated to thin films, which facilitates its surface modification. Our paper on MRO, thus, provides a template to realize ferromagnetism in vdW materials with multitype transition metals.

DOI: [10.1103/PhysRevB.104.075133](https://doi.org/10.1103/PhysRevB.104.075133)

I. INTRODUCTION

Magnetic van der Waals (vdW) materials have been intensively studied recently due to their appealing physical properties and potential applications in spintronics [1]. So far, a considerable number of intrinsic ferromagnetic (FM) or antiferromagnetic (AFM) vdW materials containing transition-metal (TM) ions have been found, such as CrI_3 [2], CrBr_3 [3,4], CrCl_3 [4,5], $\text{Cr}_2\text{Ge}_2\text{Te}_6$ [6], Fe_3GeTe_2 [7], FePS_3 [8], *et al.* The weak interlayer interactions in these magnetic vdW materials make them easy to be exfoliated down to the thin-film forms with stable magnetic order [9], which can provide a platform to study low-dimensional magnetism and are beneficial for the device miniaturization.

In TM compounds, several mechanisms have been proposed for an FM coupling. Based on the Goodenough-Kanamori-Anderson (GKA) rule [10–12], the interaction between TM atoms is predicted to be FM when the TM-ligand-TM bond angle is near 90° but strong AFM when the bond angle is around 180° . The ferromagnetism can be also induced by the Ruderman-Kittel-Kasuya-Yosida [13–15] interaction via itinerant carriers at moderate TM-TM distance or by the Zener's double exchange [16–18] between the mixed-valence TM atoms. Moreover, the Zener's *p-d* exchange [19] can lead to the ferromagnetism in dilute magnetic semiconductors (DMS). In addition to the above mechanisms that

mainly focus on the compounds with one type of TM atoms, the ferromagnetic coupling can also appear in double perovskites $\text{A}_2\text{BB}'\text{O}_6$ that contain two kinds of TM atoms, such as A_2FeMoO_6 ($A = \text{Ca}, \text{Sr}, \text{Ba}$) [20–23], A_2FeReO_6 ($A = \text{Ca}, \text{Sr}$) [21,24], A_2CrReO_6 ($A = \text{Ca}, \text{Sr}$) [25,26], and Sr_2CrWO_6 [27]. The strong AFM superexchange between neighboring B and B' ions with different magnetic moments results in an effective ferromagnetic coupling between the B atoms by means of the B-O-B'-O-B superexchange. However, because of the similar crystal fields of BO_6 and $\text{B}'\text{O}_6$ octahedrons, the antisite disorder (B' in the B site, for example) is usually inevitable in real double perovskites [28–31]. Even so, the realization of ferromagnetism in double perovskites inspires us to explore the ferromagnetic vdW material analogs.

One may expect that a ferromagnetic vdW material takes the advantages of above properties: a strong FM coupling via the similar B-O-B'-O-B superexchange and no antisite disorder. Here, we propose that the anhydrous perrhenate $\text{Mn}(\text{ReO}_4)_2$ [32] (MRO) (Fig. 1) may provide such a possibility. Similar to a double perovskite, MRO contains two kinds of TM atoms. Although MRO was reported to be a weakly AFM insulator [32], an FM coupling between two nearest-neighbor (NN) Mn atoms may be induced via the Mn-O-Re-O-Mn superexchange by charge doping. In fact, charge doping has been widely used to not only induce the magnetic states in three-dimensional DMS [19,33–35] and two-dimensional nonmagnetic vdW materials [36–39], but also tune the different magnetic transitions in magnetic compounds, such as $(\text{Sr}_{1-x}, \text{A}_x)_2\text{MnGe}_2\text{S}_6\text{O}$ ($A = \text{K}, \text{La}$) [40] and CrI_3 [41]. In consideration of the layered structure of MRO, it is also conducive for intercalating charge reservoir

*These authors contributed equally to this work.

†kliu@ruc.edu.cn

‡zlu@ruc.edu.cn

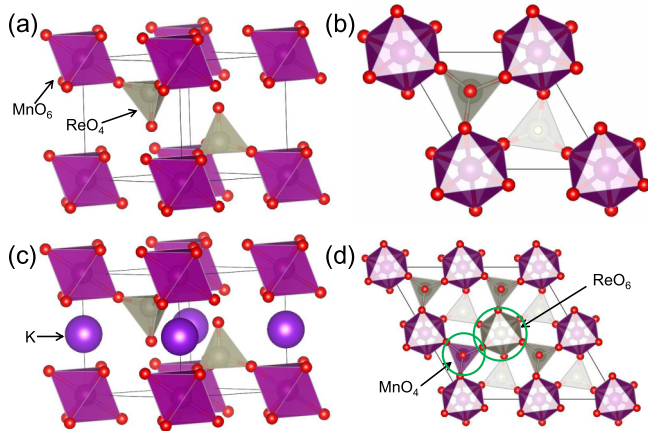


FIG. 1. (a) Side view and (b) top view of the crystal structures of MRO in which the MnO_6 octahedra (purple) are connected by the ReO_4 tetrahedra (gray). (c) Side view of the crystal structure of K-intercalated MRO. The K atoms locate at the coordinate of (0, 0, 0.5). (d) Top view of the $2 \times 2 \times 1$ supercell of MRO with an antisite defect highlighted by green circles.

layers. Furthermore, the Mn and Re atoms are in a MnO_6 octahedron and a ReO_4 tetrahedron, respectively, for which the different coordination environments may preclude their antisite mixing.

In this paper, we have systematically studied the charge doping effect on the magnetic properties and the electronic structures of MRO by using density functional theory (DFT) calculations. We find that the electron doping, rather than the hole doping, can suppress the weak AFM order in MRO and further induce an FM order in the doped compound. With increasing the electron doping, the FM ground state becomes more and more robust. The low cleavage energy and strong magnetic anisotropy of MRO suggest that the electron-doped MRO is an FM vdW material which can be exfoliated to thin films. Our theoretical predictions on MRO call for future experimental verification.

II. COMPUTATIONAL DETAILS

The first-principles electronic structure calculations on undoped and doped MRO were performed by using the projector augmented-wave method [42,43] as implemented in the Vienna *ab initio* simulation package [44–46]. The generalized gradient approximation (GGA) of Perdew-Burke-Ernzerhof type was adopted for the exchange-correlation functional [47]. The kinetic-energy cutoff of the plane-wave basis was set to be 520 eV. The $8 \times 8 \times 8$, $8 \times 8 \times 4$, and $4 \times 4 \times 8$ Monkhorst-Pack \mathbf{k} meshes were used for the Brillouin zone sampling of the primitive cell, the $1 \times 1 \times 2$ supercell, and the $\sqrt{3} \times \sqrt{3} \times 1$ supercell, respectively. The interlayer vdW interaction was described by using the DFT-D3 method of Grimme [48]. The strong correlation effect among the Mn^{2+} $3d$ electrons was considered with the on-site Coulomb repulsion (effective Hubbard $U = 4$ eV), similar to the case of Fe^{3+} in $\text{RbFe}(\text{MoO}_4)_2$ [49]. Spin-orbital coupling (SOC) was also considered in this calculation. Two approaches were adopted to simulate the charge doping effect: one is by changing the

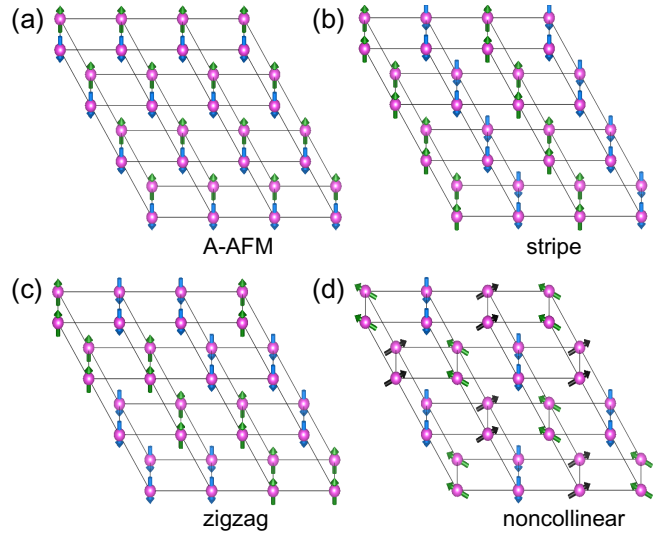


FIG. 2. Three typical collinear and one noncollinear spin configurations of Mn atoms in bulk MRO: (a) A-type antiferromagnetic (A-AFM) state with intralayer FM and interlayer AFM couplings, (b) intralayer stripe AFM, (c) intralayer zigzag AFM, and (d) intralayer noncollinear AFM state with interlayer FM coupling, respectively.

total number of electrons of the system with a compensating jellium background, and the other is by intercalating K atoms to the interlayer positions [Fig. 1(c)] according to the structure of $\text{RbFe}(\text{MoO}_4)_2$ [50]. For the former, the lattice constants were fixed at their experimental values ($a = b = 5.8579$, $c = 6.0665$ Å) [32] whereas the internal atomic positions were fully relaxed until the forces on all atoms were smaller than 0.01 eV/Å. For $\text{KMn}(\text{ReO}_4)_2$, both the lattice parameters and the atomic positions were optimized. The phonon spectra were calculated using the QUANTUM ESPRESSO package [51] in which the \mathbf{k} meshes and \mathbf{q} meshes were selected as $12 \times 12 \times 1$ and $6 \times 6 \times 1$, respectively, for the primitive cell of MRO.

III. RESULTS AND ANALYSIS

The anhydrous perrhenate MRO has an undulating layered structure [Fig. 1(a)]. In each layer, the MnO_6 octahedra are linked together with the corner-sharing ReO_4 tetrahedra, while the Mn atoms in the same layer form a frustrated triangle lattice with an Mn-Mn distance of 5.86 Å [Fig. 1(b)]. MRO is reported to be AFM with a T_N of 3.1 K [32]. The Mn atom is in the high-spin state ($3d^5$, $S = 5/2$), and the Re atom is spinless. To examine the magnetic ground state of MRO theoretically, we considered six typical magnetic configurations for the Mn spins: the nonmagnetic (NM) state, the FM state, and four possible AFM states (Fig. 2), namely, the A-type AFM (A-AFM), the stripe AFM (stripe), the zigzag AFM (zigzag), and the noncollinear AFM (noncollinear) states. The calculated relative energies of these states are listed in Table I. As can be seen, all these magnetic states are energetically more stable than the nonmagnetic state. Meanwhile, the energy differences among those magnetic states are subtle. In particular, the negligible energy

TABLE I. The energy differences E (in units of meV/Mn) of different magnetic configurations with respect to the FM state for undoped MRO and the local magnetic moments on Mn and Re atoms (in units of μ_B) calculated by the GGA + SOC + U method. The noncollinear AFM state is abbreviated to “NCL”.

Undoped	NM	FM ^z	A-AFM ^z	Stripe ^z	Zigzag ^z	NCL
E	4906.39	0	4.24	-0.80	-1.17	-2.67
M_{Mn}		4.56	4.56	4.55	4.55	4.55
M_{Re}		0.09	0.09	0.03	0.03	0

difference between the FM and the A-AFM states indicate that the interlayer magnetic coupling in MRO is very weak. As to the intralayer interaction, we find that the noncollinear AFM state with the Mn spins forming the 120° structure in the ab plane [as shown in Fig. 2(d)] is energetically slightly lower (2.67 meV/Mn) than the FM state. The small energy differences among the magnetic states also imply a low Néel temperature, which is in accord with the experimental measurements on MRO ($T_N = 3.1$ K) [32] and its analog $\text{RbFe}(\text{MoO}_4)_2$ ($T_N = 3.8$ K) [52].

We next studied the effect of charge doping on the magnetic properties of MRO. Table II shows the energy differences among the aforementioned spin magnetic states at several doping concentrations. With a charge doping of 0.5 electrons per formula unit ($e/f.u.$), the FM state becomes the magnetic ground state, which is energetically about 50.86 meV/Mn lower than that of the noncollinear state and 1.36 meV/Mn lower than that of the A-AFM state, respectively. This indicates that the electron doping can induce both intralayer and interlayer FM couplings. When the doping concentration increases to 1.0 $e/f.u.$, the FM state is still the ground state with a reinforced interlayer FM coupling. In addition to the pure charge doping, the K-doped MRO [Fig. 1(c)] as inspired by the crystal structure of $\text{RbFe}(\text{MoO}_4)_2$ [50] provides another feasible approach to realize electron doping. From the calculated energy differences listed in Table III, the situation of $\text{KMn}(\text{ReO}_4)_2$ (KMRO) is quite similar to that with the pure electron doping (Table II). On the other hand, we also investigated the case of hole doping. At a doping concentration of 0.5 $h/f.u.$ (Table II), the energy differences among the magnetic states are negligible, making it difficult for the FM state to stand out. These results suggest that it is the electron doping rather than the hole doping that can effectively suppress the original AFM order and induce an FM order in MRO.

To understand the role of charge doping playing in the AFM-FM transition, we further made a comparison study on the electronic structures of MRO and KMRO. The spin densities, the differential charge densities, and the partial density of states for the atoms, whose orbitals have main contributions around the Fermi level, are shown in Fig. 3. For the undoped MRO, due to the strong electronegativity of the tetrahedral $[\text{ReO}_4]^-$ ionic groups, the $3d$ orbitals of Mn^{2+} ions are half-occupied ($3d^5$), leading to an insulating noncollinear AFM state with a band gap of 2.5 eV. As can be seen from Fig. 3(a), the valence bands mainly consist of Mn- $3d$ and O- $2p$ orbitals, whereas the conduction bands

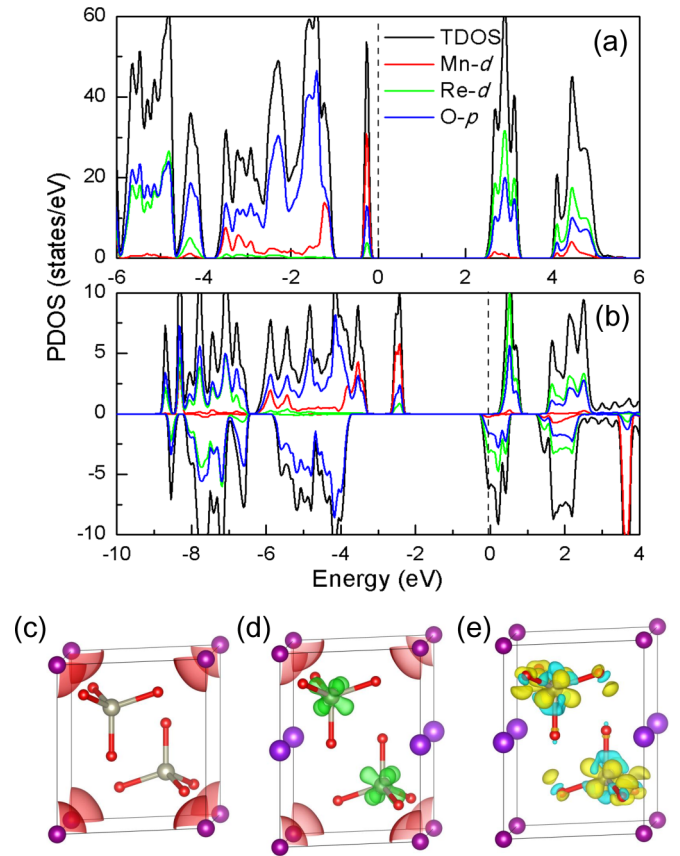


FIG. 3. Total and local density of states for (a) the noncollinear AFM state of MRO and (b) the FM state of KMRO calculated with GGA + U . The Fermi level sets to zero. Spin densities for the ferromagnetic states of (c) MRO and (d) KMRO. The kermesinus and green isosurfaces show the spin-up and spin-down densities, respectively. (e) Differential charge densities with the intercalation of K ions ($\rho_{\text{KMRO}} - \rho_{\text{MRO}} - \rho_{\text{K}}$). The yellow and cyan isosurfaces show the electron accumulation and depletion areas, respectively.

are primarily contributed by Re- $5d$ and O- $2p$ orbitals. The common peaks of these orbitals in the same energy range near the Fermi level indicate the strong p - d hybridizations. In addition, the Mn atoms have the local magnetic moments of about $4.55\mu_B$, and the Re atoms are not spin polarized (Table I). The magnetic interactions between the Mn atoms are very weak due to the large Mn-Mn distance (5.86 Å). As for KMRO [Fig. 3(b)], the electron doping effect induced by the K intercalation is twofold: It not only shifts the Fermi level upwards, but also introduces the electrons into the Re- $5d$ and O- $2p$ orbitals [Figs. 3(b) and 3(e)]. Moreover, the orbitals of K atoms are far away from the Fermi level, whereas the five $3d$ electrons of Mn^{2+} ions fully occupy the spin-up channel and leave the spin-down channel empty. As a result, the Re atoms become spin polarized [Figs. 3(c) and 3(d)] with small local moments of $-0.23\mu_B$ (Table III), which are antiparallel to those of Mn atoms ($M_{\text{Mn}} = 4.49\mu_B$). The Mn-O-Re bond angle is 157° [32], so there exists the intralayer AFM superexchange in electron-doped MRO according to the GKA rules, which then leads to robust FM interactions between the Mn atoms via the Mn-O-Re-O-Mn bridge, analogous to the case of double-perovskite $\text{Sr}_2\text{FeReO}_6$ [24].

TABLE II. The energy differences E (in units of meV/Mn) of different magnetic configurations with respect to the FM state for bulk MRO at several doping concentrations and the local magnetic moments on Mn and Re atoms (in units of μ_B) calculated by the GGA + SOC + U method. The noncollinear AFM state is abbreviated to “NCL”.

Doping		FM ^z	A-AFM ^z	Stripe ^z	Zigzag ^z	NCL
0.5 e/f.u.	E	0	1.36	37.81	39.10	50.86
	M_{Mn}	4.51	4.51	4.52	4.52	4.52
	M_{Re}	0.07	0.06	0.08	0.07	0
1.0 e/f.u.	E	0	1.40	83.45	70.71	109.44
	M_{Mn}	4.47	4.46	4.48	4.48	4.49
	M_{Re}	0.22	0.21	0.20	0.20	0
0.5 h/f.u.	E	0	0.47	-0.79	-0.37	-0.57
	M_{Mn}	4.24	4.24	4.23	4.26	4.27
	M_{Re}	0.07	0.07	0.02	0.02	0

In addition, we investigated the magnetic anisotropic energies (MAE) for the FM state of electron-doped MRO. In reference to the energy of the off-plane spin moment direction, the calculated MAE along some low index facets are listed in Table IV. It can be seen that the MAE of electron-doped MRO is much larger than those of most FM materials (0.43 meV/Fe for bulk Fe₃GeTe₂ [53], 0.14 meV/Fe for elemental iron [54], 0.12 meV/Ni for elemental nickel [54]) and the magnetic easy axes of both two kinds of electron-doped MRO are along the $\langle 001 \rangle$ direction. We have utilized different Hubbard U values, which does not change the results.

In order to evaluate the stability of the FM ordering of KMRO, the Curie temperature (T_c) is predicted based on the classical Heisenberg model. The magnetic coupling Hamiltonian can be written as

$$H = J_1 \sum_{\langle i,j \rangle} \vec{S}_i \cdot \vec{S}_j + J_2 \sum_{\langle\langle i,j \rangle\rangle} \vec{S}_i \cdot \vec{S}_j + J_3 \sum_{\langle\langle\langle i,j \rangle\rangle\rangle} \vec{S}_i \cdot \vec{S}_j + J_c \sum_{\langle i,j \rangle} \vec{S}_i \cdot \vec{S}_j + \sum_i A_i (\vec{S}_i \cdot \vec{e}_i)^2. \quad (1)$$

Here, S_i is the spin of the Mn atom, A_i is the single-ion anisotropy at spin S_i , \vec{e}_i is the unit vector pointing along the direction of the easy-magnetization axes, J_c is the out-of-plane NN exchange interaction, J_n ($n = 1-3$) are in-plane NN, next-nearest-neighbor, and third-nearest-neighbor exchange interactions of Mn atoms (inset of Fig. 4), respectively. Based on the energy differences of FM and different AFM states for KMRO (Tables III and IV), we extract the magnetic coupling parameters calculated with different U values as shown in Fig. 4. The NN exchange J_1 is FM, whereas other in-plane

TABLE III. The energy differences E (in units of meV/Mn) of different magnetic configurations with respect to the FM state for bulk KMRO and the local magnetic moments on Mn and Re atoms (in units of μ_B) calculated by the GGA + SOC + U method. The noncollinear AFM state is abbreviated to “NCL”.

KMRO	NM	FM ^z	A-AFM ^z	Stripe ^z	Zigzag ^z	NCL
E	3751.41	0	2.13	79.39	69.23	105.33
M_{Mn}		4.49	4.49	4.50	4.50	4.51
M_{Re}		0.23	0.22	0.24	0.22	0.01

J_2 , J_3 , and out-of-plane J_c are much smaller. Thus, the Curie temperature can be expressed as [55]

$$k_B T_c = \frac{4\sqrt{3}}{3} \frac{S+1}{S} \frac{J_1 S^2}{\ln\left(\frac{\Delta + \sqrt{3}J_1 S^2}{\Delta}\right)}. \quad (2)$$

Here, $\Delta = AS^2$ is the magnetocrystalline anisotropy, and $S = 5/2$. The calculated T_c 's of KMRO are shown in Fig. 4. For $U = 4$ eV, T_c is about 310 K, well above room temperature.

Since MRO has an undulating layered structure, we also calculated the cleavage energy of MRO to estimate its exfoliation feasibility [Fig. 5(a)]. Several different approaches, including the DFT-D2 [56] and DFT-D3 [48] methods, were used to describe the interlayer vdW interactions. The maximal value of the calculated cleavage energies is 0.582 J/m² by using the DFT-D2 method, which is slightly larger than that (0.37 J/m²) of graphite [57]. Meanwhile, there is no imaginary-frequency mode in the phonon spectra of the MRO monolayer as shown in Fig. 5(b), which indicates its dynamical stability. In comparison, Park's group demonstrated that another undulating layered material Pd₃P₂S₈ can be exfoliated down to the monolayer [58]. These results imply that we may explore MRO with reduced dimensions, which provides an opportunity to tune its properties more effectively, for example, via surface functionalization or ion liquid gating technique.

IV. DISCUSSION AND SUMMARY

The most prominent feature of anhydrous perrhenate KMRO is that the electron doping via the K intercalation leads to the Mn-O-Re AFM superexchange and then results in an effective FM coupling between the Mn atoms through the Mn-O-Re-O-Mn bridge. Since the local magnetic moments on the Mn atoms (about $4.5\mu_B$) are much larger than those on the Re atoms (about $-0.2\mu_B$), KMRO can be considered to be FM as

TABLE IV. The MAEs (in units of meV/Mn) of electron-doped MRO along some low index facets.

MAE	$\langle 001 \rangle$	$\langle 100 \rangle$	$\langle 010 \rangle$	$\langle 110 \rangle$	$\langle 1\bar{1}0 \rangle$
1.0 e/f.u.	0	8.869	8.869	8.868	6.373
KMRO	0	6.934	7.767	7.771	7.779

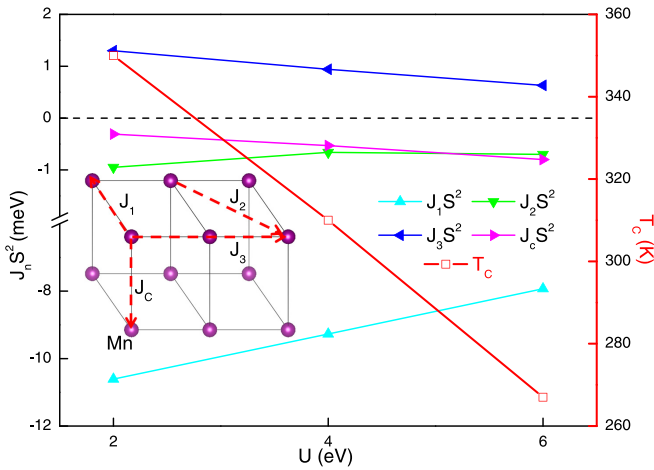


FIG. 4. Curie temperature (T_c) and Heisenberg exchange interactions $J_n S^2$ calculated with different Hubbard U values. The inset shows the schematic of the magnetic couplings J_n ($n = 1-3, c$) among Mn^{2+} ions.

a whole. Especially, the electrons introduced by the K atoms are mainly doped into the Re- d orbitals due to the strong Coulomb repulsion for double occupation of Mn- d orbitals. In contrast, for the hole-doped MRO with a doping concentration of 0.5 h/f.u. (Table II), the hole-type carriers come from the Mn- d orbitals and the local magnetic moments on Re atoms are still zero, i.e., the Mn-O-Re AFM superexchange being not well established. Hence, the energy difference between the FM and the AFM states of the hole-doped MRO is negligible. According to our calculation results, it is also worth noting that the FM state is not the ground state if part of the Re atoms in MRO are substituted by Os atoms, even though the electron doping seems equivalent to that in KMRO. This is because that in partially substituted $\text{Mn}(\text{Re}_{1-x}\text{Os}_x\text{O}_4)_2$ ($0 < x < 1$), the local magnetic moments locate at Mn and Os atoms, whereas the local moments of Re atoms still remain zero. Thus, a uniform electron doping on the Re atoms is necessary to link the Mn atoms together to form a long-range FM order.

On the other hand, there may exist antisite defects in the real materials with multiple transition-metal ions. In order to figure out the antisite structure of MRO similar to the case of a double perovskite, we chose a $2 \times 2 \times 1$ supercell containing four chemical formula by exchanging one pair of the Re and Mn sites [as shown in Fig. 1(d)]. Different from the double perovskites $A_2\text{BB}'\text{O}_6$ in which both B and B' form octahedrons, the Re and Mn atoms in MRO are in different crystal fields: the former in tetrahedron and the latter in octahedron configurations. We find that the antisite structure of MRO has a rather higher energy (about 0.615 eV/f.u.) than that of the normal one. This suggests that the antisite disorder in MRO could be avoided via fine control of experimental conditions.

MRO has several advantages as a parent compound for inducing high- T_c ferromagnetism. First, it is a vdW material that

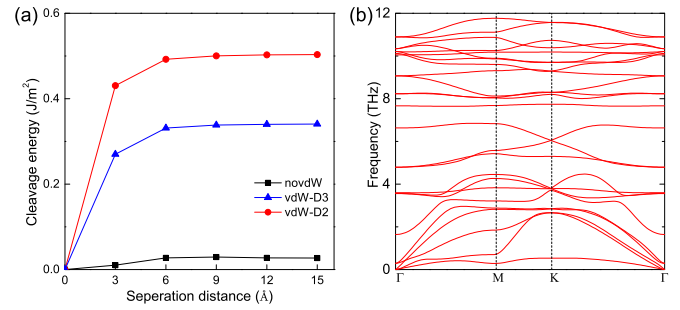


FIG. 5. (a) Cleavage energy of MRO calculated with different methods to include the vdW interactions. (b) Phonon spectra of the MRO monolayer.

could be exfoliated down to monolayer, which facilitates the surface modification or charge doping. Second, the FM order in uniformly electron-doped MRO (such as KMRO) derived from the strong Mn-O-Re AFM superexchange is very robust. Third, the large MAE of MRO is beneficial for stabilizing the low-dimensional magnetic long-range order. Fourth, the Mn and Re atoms in MRO have a small possibility to form antisite disorder, which is conducive to improve the sample quality.

To summarize, we have investigated the magnetic properties and the electronic structures of the electron-doped anhydrous perhenate MRO by using first-principles calculations. Due to the inherent crystal structure with the relatively long Mn-Mn distance separated by nonmagnetic ReO_4 tetrahedra, the magnetic couplings among the Mn atoms in pristine MRO are very weak. By introducing moderate electrons into the Re- d orbitals, the Mn-O-Re AFM superexchange channel opens accompanied with an effective FM coupling between the Mn atoms, leading to a long-range FM order with the calculated Curie temperature above 300 K. Our studies show that the electron-doped MRO may provide a prototype system to explore high- T_c FM materials that are derived from an intrinsic AFM insulator with multiple kinds of transition-metal ions.

ACKNOWLEDGMENTS

We wish to thank C. Wang for helpful discussions. This work was supported by the National Key R&D Program of China (Grants No. 2017YFA0302903 and No. 2019YFA0308603), the National Natural Science Foundation of China (Grants No. 11774424 and No. 11934020), the Beijing Natural Science Foundation (Grant No. Z200005), the CAS Interdisciplinary Innovation Team, the Fundamental Research Funds for the Central Universities (CN), and the Research Funds of Renmin University of China (Grant No. 19XNLG13). Computational resources were provided by the Physical Laboratory of High Performance Computing at Renmin University of China and Shanghai Supercomputer Center.

[1] I. Žutić, J. Fabian, and S. Das Sarma, *Rev. Mod. Phys.* **76**, 323 (2004).

[2] Y. Liu and C. Petrovic, *Phys. Rev. B* **97**, 014420 (2018).

- [3] C. Jin, Z. Tao, K. Kang, K. Watanabe, T. Taniguchi, K. F. Mak, and J. Shan, *Nature Mater.* **19**, 1290 (2020).
- [4] H. H. Kim, B. Yang, S. Li, S. Jiang, C. Jin, Z. Tao, G. Nichols, F. Sfigakis, S. Zhong, C. Li, S. Tian, D. G. Cory, G. X. Miao, J. Shan, K. F. Mak, H. Lei, K. Sun, L. Zhao, and A. W. Tsen, *Proc. Natl. Acad. Sci. USA* **116**, 11131 (2019).
- [5] D. R. Klein, D. MacNeill, Q. Song, D. T. Larson, S. Fang, M. Xu, R. A. Ribeiro, P. C. Canfield, E. Kaxiras, R. Comin, and P. Jarillo-Herrero, *Nat. Phys.* **15**, 1255 (2019).
- [6] C. Gong, L. Li, Z. Li, H. Ji, A. Stern, Y. Xia, T. Cao, W. Bao, C. Wang, Y. Wang, Z. Q. Qiu, R. J. Cava, S. G. Louie, J. Xia, and X. Zhang, *Nature (London)* **546**, 265 (2017).
- [7] Z. Fei, B. Huang, P. Malinowski, W. Wang, T. Song, J. Sanchez, W. Yao, D. Xiao, X. Zhu, A. F. May, W. Wu, D. H. Cobden, J. H. Chu, and X. Xu, *Nature Mater.* **17**, 778 (2018).
- [8] A. Wiedenmann, J. Rossat-Mignod, A. Louisy, R. Brec, and J. Rouxel, *Solid State Commun.* **40**, 1067 (1981).
- [9] N. Miao, B. Xu, L. Zhu, J. Zhou, and Z. Sun, *J. Am. Chem. Soc.* **140**, 2417 (2018).
- [10] J. B. Goodenough, *Phys. Rev.* **100**, 564 (1955).
- [11] J. Kanamori, *J. Appl. Phys.* **31**, S14 (1960).
- [12] P. W. Anderson, *Phys. Rev.* **115**, 2 (1959).
- [13] M. A. Ruderman and C. Kittel, *Phys. Rev.* **96**, 99 (1954).
- [14] T. Kasuya, *Prog. Theor. Phys.* **16**, 45 (1956).
- [15] K. Yosida, *Phys. Rev.* **106**, 893 (1957).
- [16] C. Zener, *Phys. Rev.* **82**, 403 (1951).
- [17] P. W. Anderson and H. Hasegawa, *Phys. Rev.* **100**, 675 (1955).
- [18] P. G. de Gennes, *Phys. Rev.* **118**, 141 (1960).
- [19] K. Sato, L. Bergqvist, J. Kudrnovsky, P. H. Dederichs, O. Eriksson, I. Turek, B. Sanyal, G. Bouzerar, H. Katayama-Yoshida, V. A. Dinh, T. Fukushima, H. Kizaki, and R. Zeller, *Rev. Mod. Phys.* **82**, 1633 (2010).
- [20] Y. Tomioka, T. Okuda, Y. Okimoto, R. Kumai, K. I. Kobayashi, and Y. Tokura, *Phys. Rev. B* **61**, 422 (2000).
- [21] Z. Szotek, W. M. Temmerman, A. Svane, L. Petit, G. M. Stocks, and H. Winter, *J. Magn. Magn. Mater.* **272–276**, 1816 (2004).
- [22] R. P. Borges, R. M. Thomas, C. Cullinan, J. M. D. Coey, R. Suryanarayanan, L. Ben-Dor, L. Pinsard-Gaudart, and A. Revcolevschi, *J. Phys.: Condens. Matter* **11**, L445 (1999).
- [23] J. Gopalakrishnan, A. Chattopadhyay, S. B. Ogale, T. Venkatesan, R. L. Greene, A. J. Millis, K. Ramesha, B. Hannoyer, and G. Marest, *Phys. Rev. B* **62**, 9538 (2000).
- [24] K. I. Kobayashi, T. Kimura, Y. Tomioka, H. Sawada, K. Terakura, and Y. Tokura, *Phys. Rev. B* **59**, 11159 (1999).
- [25] A. J. Hauser, J. R. Soliz, M. Dixit, R. E. A. Williams, M. A. Susner, B. Peters, L. M. Mier, T. L. Gustafson, M. D. Sumption, H. L. Fraser, P. M. Woodward, and F. Y. Yang, *Phys. Rev. B* **85**, 161201(R) (2012).
- [26] H. Kato, T. Okuda, Y. Okimoto, Y. Tomioka, Y. Takenoya, A. Ohkubo, M. Kawasaki, and Y. Tokura, *Appl. Phys. Lett.* **81**, 328 (2002).
- [27] J. B. Philipp, P. Majewski, L. Alff, A. Erb, R. Gross, T. Graf, M. S. Brandt, J. Simon, T. Walther, W. Mader, D. Topwal, and D. D. Sarma, *Phys. Rev. B* **68**, 144431 (2003).
- [28] J. Navarro, L. Balcells, F. Sandiumenge, M. Bibes, A. Roig, B. Martínez, and J. Fontcuberta, *J. Phys.: Condens. Matter* **13**, 8481 (2001).
- [29] L. Fuoco, D. Rodriguez, T. Poppel, and P. A. Maggard, *Chem. Mater.* **23**, 5409 (2011).
- [30] A. S. Ogale, S. B. Ogale, R. Ramesh, and T. Venkatesan, *Appl. Phys. Lett.* **75**, 537 (1999).
- [31] T. Saha-Dasgupta and D. D. Sarma, *Phys. Rev. B* **64**, 064408 (2001).
- [32] C. C. Torardi, W. M. Reiff, B. C. Dodrill, and T. Vogt, *Mat. Res. Soc. Symp. Proc.* **453**, 399 (1997).
- [33] C. Ding, H. Y. Man, C. Qin, J. C. Lu, Y. L. Sun, Q. Wang, B. Q. Yu, C. M. Feng, T. Goko, C. J. Arguello, L. Liu, B. A. Frandsen, Y. J. Uemura, H. D. Wang, H. Luetkens, E. Morenzoni, W. Han, C. Q. Jin, T. Munsie, T. J. Williams *et al.*, *Phys. Rev. B* **88**, 041102(R) (2013).
- [34] K. Zhao, Z. Deng, X. C. Wang, W. Han, J. L. Zhu, X. Li, Q. Q. Liu, R. C. Yu, T. Goko, B. Frandsen, L. Liu, F. Ning, Y. J. Uemura, H. Dabkowska, G. M. Luke, H. Luetkens, E. Morenzoni, S. R. Dunsiger, A. Senyshyn, and P. Böni, and C. Q. Jin, *Nat. Commun.* **4**, 1442 (2013).
- [35] Z. Deng, C. Q. Jin, Q. Q. Liu, X. C. Wang, J. L. Zhu, S. M. Feng, L. C. Chen, R. C. Yu, C. Arguello, T. Goko, F. L. Ning, J. S. Zhang, Y. Y. Wang, A. A. Aczel, T. Munsie, T. J. Williams, G. M. Luke, T. Kakeshita, S. Uchida, W. Higemoto *et al.*, *Nat. Commun.* **2**, 422 (2011).
- [36] Y.-W. Son, M. L. Cohen, and S. G. Louie, *Nature (London)* **444**, 347 (2006).
- [37] T. Cao, Z. Li, and S. G. Louie, *Phys. Rev. Lett.* **114**, 236602 (2015).
- [38] N. Miao, B. Xu, N. C. Bristowe, J. Zhou, and Z. Sun, *J. Am. Chem. Soc.* **139**, 11125 (2017).
- [39] N. Miao, W. Li, L. Zhu, B. Xu, J. Zhou, S. R. Elliott, and Z. Sun, *Nanoscale Horiz.* **5**, 1566 (2020).
- [40] H. C. Yang, B. C. Gong, K. Liu, and Z. Y. Lu, *Science Bull.* **63**, 887 (2018).
- [41] S. Jiang, L. Li, Z. Wang, K. F. Mak, and J. Shan, *Nat. Nanotechnol.* **13**, 549 (2018).
- [42] P. E. Blöchl, *Phys. Rev. B* **50**, 17953 (1994).
- [43] G. Kresse and D. Joubert, *Phys. Rev. B* **59**, 1758 (1999).
- [44] G. Kresse and J. Hafner, *Phys. Rev. B* **47**, 558 (1993).
- [45] G. Kresse and J. Furthmüller, *Comput. Mater. Sci.* **6**, 15 (1996).
- [46] G. Kresse and J. Furthmüller, *Phys. Rev. B* **54**, 11169 (1996).
- [47] J. P. Perdew, K. Burke, and M. Ernzerhof, *Phys. Rev. Lett.* **77**, 3865 (1996).
- [48] S. Grimme, J. Antony, S. Ehrlich, and S. Krieg, *J. Chem. Phys.* **132**, 154104 (2010).
- [49] K. Cao, R. D. Johnson, F. Giustino, P. G. Radaelli, G.-C. Guo, and L. He, *Phys. Rev. B* **90**, 024402 (2014).
- [50] T. Inami, Y. Ajito, and T. Goto, *J. Phys. Soc. Jpn.* **65**, 2374 (1996).
- [51] P. Giannozzi, S. Baroni, N. Bonini, M. Calandra, R. Car, C. Cavazzoni, D. Ceresoli, G. L. Chiarotti, M. Cococcioni, I. Dabo *et al.*, *J. Phys.: Condens. Matter* **21**, 395502 (2009).
- [52] M. Kenzelmann, G. Lawes, A. B. Harris, G. Gasparovic, C. Broholm, A. P. Ramirez, G. A. Jorge, M. Jaime, S. Park, Q. Huang, A. Y. Shapiro, and L. A. Demianets, *Phys. Rev. Lett.* **98**, 267205 (2007).
- [53] Y. Wang, C. Wang, S.-J. Liang, Z. Ma, K. Xu, X. Liu, L. Zhang, A. S. Admasu, S.-W. Cheong, L. Wang, M. Chen, Z. Liu, B. Cheng, W. Ji, and F. Miao, *Adv. Mater.* **32**, 2004533 (2020).
- [54] P. Bruno, in *Magnetismus von Festkörpern und Grenzflächen* (KFA Jülich, Jülich, 1993), p. 24.1.
- [55] M. Modarresi, A. Mogulkoc, Y. Mogulkoc, and A. N. Rudenko, *Phys. Rev. Appl.* **11**, 064015 (2019).

- [56] S. Grimme, *J. Comp. Chem.* **27**, 1787 (2006).
- [57] W. Wang, S. Dai, X. Li, J. Yang, D. J. Srolovitz, and Q. Zheng, *Nat. Commun.* **6**, 7853 (2015).
- [58] S. Park, S. Kang, H. Kim, K. H. Lee, P. Kim, S. Sim, N. Lee, B. Karuppanan, J. Kim, J. Kim, K. I. Sim, M. J. Coak, Y. Noda, C. H. Park, J. H. Kim, and J. G. Park, *Sci. Rep.* **10**, 20998 (2020).